Synthesis of Nanostructured Mesoporous Manganese Oxides with Three-Dimensional Frameworks and Their Application in Supercapacitors

ARTICLE *in* THE JOURNAL OF PHYSICAL CHEMISTRY C · MARCH 2011

Impact Factor: 4.77 · DOI: 10.1021/jp110938x

THE JOURNAL OF PHYSICAL CHEMISTRY C

ARTICLE

pubs.acs.org/JPCC

Synthesis of Nanostructured Mesoporous Manganese Oxides with Three-Dimensional Frameworks and Their Application in Supercapacitors

Yu-Ting Wang, An-Hui Lu, Hui-Li Zhang, and Wen-Cui Li*

State Key Laboratory of Fine Chemicals, School of Chemical Engineering, Dalian University of Technology, Dalian 116024, China

Supporting Information

ABSTRACT: Nanostructured mesoporous manganese oxides were easily prepared by mixing $KMnO_4$ with ascorbic acid in an aqueous solution under ambient conditions. The obtained manganese oxides were identified as having an α-MnO_2 tunnel structure composed of an edge-shared network of [MnO_6] octahedra. TEM observations revealed that the obtained MnO_2 materials had three-dimensional frameworks which consisted of homogeneous nanoparticles with sizes of ca. 5 nm. Nitrogen sorption analyses showed that these MnO_2 nanoparticles exhibited a type IV isotherm, indicating a mesoporous character. Large surface areas up to 284 $m^2\ g^{-1}$ were recorded. The electrochemical performances of the synthesized α-MnO_2 nanoparticles as supercapacitor electrode materials were studied using cyclic voltammetry and galvanostatic charge−discharge cycling in a three-electrode system at a potential range from 0 to 1.0 V vs a saturated calomel electrode in 0.5 M sodium sulfate solution. The result showed that mesoporous MnO_2 with three-dimensional frameworks exhibit a high capacitance up to ∼200 F g^{-1}. Furthermore, a hybrid supercapacitor was assembled by using MnO_2 mixed with a small amount of activated carbon as the positive electrode and activated carbon as the negative electrode in a 0.5 M Na_2SO_4 electrolyte. By balancing the mass of MnO_2 and activated carbon, a practical cell voltage of 1.8 V could be obtained in aqueous medium with a capacitance of 23.1 F g^{-1}. After 1200 cycles, the maximum energy density is 10.4 Wh kg^{-1} and power density is 14.7 kW kg^{-1}. Thus, the obtained α-MnO_2 nanoparticles are suitable for use as supercapacitor electrode materials.

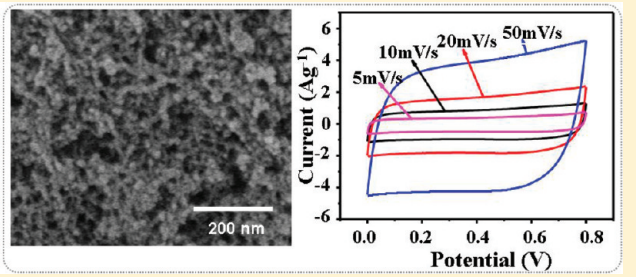

1. INTRODUCTION

Nanostructured transition metal oxides, which exhibit pseudocapacitance behavior, are considered as excellent materials in terms of achieving high specific capacitance in hybrid supercapacitors.[1−3] Among the various electrode materials used in the hybrid supercapacitors, hydrated ruthenium dioxide ($RuO_2 \cdot xH_2O$) shows the highest specific capacitance (>720 $F \cdot g^{-1}$).[4] However, its commercial use is limited because of its high cost and toxicity. Therefore, nowadays considerable efforts have been devoted to identify alternative and inexpensive electrode materials with acceptable electrochemical performance.

Manganese dioxide (MnO_2) is a good candidate thanks to its good electrochemical behavior, low cost, and environmental compatibility.[5,6] Recently, much attention has been paid to developing MnO_2-based hybrid supercapacitors. MnO_2 possesses several different crystallographic forms such as α-, β-, γ-, δ-, and ε-type, made of [MnO_6] octahedra with different connectivities. Among them, α- and δ-MnO_2 are of great interest in view of their good electrochemical capacitance behaviors.[7,8] Several routes have been reported for the synthesis of such materials, including hydrothermal reaction, thermal decomposition,[9] electro-deposition,[10] template method,[11] microemulsion method,[12] etc. In these methods, MnO_2 nanoparticles are usually prepared using $KMnO_4$ as the precursor and various inorganic compounds such as KBH_4, H_2SO_4, HCl, $K_2S_2O_4$, and Mn(II) salts as reducing agents.[13−15] Besides these inorganic salts, other organic compounds such as formamide,[16] fumaric acid,[17] aniline,[18] glucose,[19] etc. also can be used as reducing agents. However, to the best of our knowledge, most of the hitherto synthesized MnO_2 are spherical aggregate nanoparticles or spherical brushes with straight and radially grown nanorods.[7] The surface areas are usually low. There is still a lack of control of the MnO_2 morphology. Chen et al.[20] reported the synthesis of hollow spherical MnO_2, which exhibited a good electrochemical performance. Hence, MnO_2 with high surface area and mesoporosity would be useful to achieve a high capacitance and a rapid ion transfer of electrolyte in electrodes.

Ascorbic acid (AA, the chemical identity of vitamin C) is known for the reduction of chloroaurate or nitrate to generate gold nanoparticles[21] or silver nanoparticles[22] in the solution phase. However, to our knowledge, it is hard to find in literature a research work dealing with the preparation of manganese oxides

Received: November 16, 2010
Revised: February 19, 2011
Published: March 11, 2011

Table 1. Reaction Conditions for the Preparation of MnO_2

sample	molar ratio of $KMnO_4$ to AA	reaction time (min)	calcination temp (°C)
MnO_2-1	1:0.2	30	
MnO_2-2	1:0.5	30	
MnO_2-3	1:1	30	
MnO_2-4	1:1	10	
MnO_2-5	1:1	60	
MnO_2-6	1:1	30	200
MnO_2-7	1:1	30	300
MnO_2-8	1:1	30	400

using ascorbic acid as the reductant. We report herein a simple and quick synthesis of mesoporous MnO_2 nanoparticles via the reaction of potassium permanganate with ascorbic acid. Their structures were investigated by XRD, SEM, TEM, and nitrogen sorption measurements. The results reveal that the obtained MnO_2 shows a three-dimensional framework structure and has a large surface area and narrow mesopore size distribution. Electrochemical tests demonstrate these materials have a good electrochemical performance as a supercapacitor electrode.

2. EXPERIMENTAL SECTION

2.1. Sample Preparation. All chemicals used in this study are of analytical grade, and used without further purification. In a typical synthesis, 4 mmol (0.632 g) $KMnO_4$ was dissolved in 30 mL of deionized water under vigorous magnetic stirring at room temperature to form a homogeneous solution, A. Four millimoles (0.706 g) of ascorbic acid was dissolved in 20 mL of deionized water to form clear solution, B. Subsequently, solution A and solution B were mixed and aged for 30 min under continuous stirring at ambient temperature (~25 °C). After reaction, the products were collected and washed 3 times with deionized water and 2 times with absolute ethanol, and then dried at 90 °C overnight in a box oven. The reaction conditions such as the molar ratio of $KMnO_4$ to ascorbic acid, reaction time, and calcined temperature had a significant impact on the particle size. The corresponding variation in surface properties and electrochemical properties were studied elaborately and discussed in detail. The stability of these nanoparticles was also investigated. The synthesis conditions are listed in Table 1.

2.2. Characterization. Power X-ray diffraction (XRD) analysis was conducted using the Philips X'pert PRO X-ray diffractometer equipped with a Cu Kα radiation source (λ = 1.5418 Å). Scanning electron microscopy (SEM) was carried out with a JEOL microscope model JSM-6700F. High resolution transmission electron microscopy (HRTEM) investigations were performed in a Hitachi HF2000 microscope equipped with a cold field emission gun at a beam energy of 200 kV. Samples were dispersed on a copper mesh. Thermogravimetric analysis (TGA) was carried out in the temperature range from room temperature to 600 °C in air with a heating rate of 10 °C min^{-1} using a STA 449 F3 Jupiter thermogravimetric analyzer (NETZSCH). Surface area and porosity were determined by nitrogen adsorption at 77 K using a Micromeritics ASAP 2020 Analyzer. Prior to analysis, all samples were degassed under vacuum at 80 °C for at least 4 h. The specific surface area was calculated using the BET method, while the pore size distribution (PSD) curves were calculated from the desorption branches based on the Barrett–Joyner–Halenda (BJH) equation.

2.3. Electrode Preparation and Evaluation. The working electrodes of electrochemical capacitors were fabricated by mixing MnO_2 powder with 20 wt % acetylene black conductor and a 10 wt % poly(tetrafluoroethylene) (PTFE) binder. A small amount of ethanol was then added to this mixture followed by an ultrasonication treatment for 1 h. The homogenized mixture was pressed onto a stainless steel (SS) current collector (1.0 × 1.0 cm^2) to fabricate an electrode.

The electrochemical performances of MnO_2-based electrodes were tested using a cyclic voltammetry (CV) method and a constant current charge/discharge test. All electrochemical measurements were carried out in 0.5 M Na_2SO_4 aqueous electrolyte solution at room temperature with a conventional three-electrode electrochemical setup in which the MnO_2 electrode served as working electrode, and a slice of platinum sheet was used as auxiliary electrode and a saturated calomel electrode (SCE) as reference electrode. All electrochemical experiments were carried out at room temperature. Discharge specific capacitance (C) of MnO_2 was calculated using the following formula:

$$C(F/g) = It/(m\Delta E)$$

where I is the current in amps used for charge/discharge cycling, t is time in seconds of discharge, m is mass in grams of the active material, and ΔE is the operating potential window in volts of charge or discharge.

Besides evaluation in the three-electrode system, the electrochemical properties of MnO_2 in the two-electrode system have also been conducted by using commercial activated carbon (AC) as negative electrode and MnO_2 as positive electrode in 0.5 M Na_2SO_4 electrolyte. The negative electrode was prepared using AC (YP/47, specific surface area of ca. 1870 m^2 g^{-1}, Japan) mixed with acetylene black and poly(tetrafluoroethylene) (PTFE) in a weight ratio of 85:10:5 pressed onto a stainless steel grid. The positive electrode was prepared by pressing a powdered mixture of MnO_2, AC, acetylene black, and PTFE in a weight ratio of 75:10:10:5 onto a stainless steel grid. A two-electrode cell was tested on Arbin SCTS-5 V5A 8.

3. RESULTS AND DISCUSSION

Ascorbic acid (AA) is a highly polar compound and is generally thought of as containing a carboxylic acid group, although no free carboxylic group is actually present. A carboxyl group has been lost to the lactone structure. Rather, the hydroxyl groups on carbon 2 and 3 are ionizable. In particular, the hydroxyl group on carbon 3 has a pK_a of 4.04; therefore, the initial solution exhibits low acidity. We hypothesized that ascorbic acid and its ionized form may reduce MnO_4^- due to the presence of OH groups while themselves becoming the two-electron oxidized form of ascorbic acid, dehydroascorbic acid (DHA). DHA is relatively unstable and is easily converted to 2,3-diketo-1-gulonic acid (DGA) with hydrolysis of the lactone ring.[23] In the end, MnO_2 and KOH are generated, and the solution turns weakly alkaline (pH ca.9). Scheme 1 shows the proposed reaction steps.

In the experiments, we found that this reaction proceeds quickly. In order to control or tune the nanostructure of the product MnO_2, the molar ratio of $KMnO_4$ to ascorbic acid and reaction time were varied. The thermal stability of MnO_2 was also investigated.

3.1. Effect of the Amount of Ascorbic Acid on the Structure of MnO_2. The samples MnO_2-1, MnO_2-2, and MnO_2-3 were prepared at a molar ratio of $KMnO_4$ to ascorbic acid of 1:0.2, 1:0.5, and 1:1, respectively. The crystal phase and particle size of the as-prepared MnO_2 were characterized by powder XRD. As seen in Figure 1, the XRD patterns of the as-prepared MnO_2 nanoparticles exhibit clear and broad reflections at ca. 36 and 65°, and are thus suggest that these samples are in a poorly crystalline state with a short-range crystallographic form (JCPDS no. 44-0141). The broad reflections indicate that the particle sizes of the samples are small. The crystallite sizes of the particles estimated by the Scherrer formula are compiled in Table 2. It can be seen that as the amount of ascorbic acid increases, the particles sizes become smaller.

However, in the experiments, when the molar ratio of $KMnO_4$ to ascorbic acid increase to1:1.2 and 1:1.5, the reaction proceeds so fast that the solution changes to ivory-white in color due to overoxidation, and no brown-black manganese dioxide is obtained.

The morphologies of the products were investigated using SEM. As seen in Figure 2, SEM images of MnO_2-1 (Figure 2a,b) and MnO_2-3 (Figure 2c,d) show that the samples mainly consist of pseudospherical nanoparticles, which connect into chain-like structures. The particle size of MnO_2-3 is significantly smaller than that of MnO_2-1, indicating that an increase in ascorbic acid used results in a smaller particle size. These results are in agreement with the mechanism of the nucleation and growth of crystals. When the concentration of ascorbic acid increases, the number of nuclei thus increases. After the initial fast nucleation stage, the number of nanocrystals remains constant in the following diffusion-controlled growth. Therefore, the final size

Scheme 1. Plausible Formation Mechanism of Porous MnO_2 Nanoparticles Using AA as the Reductant

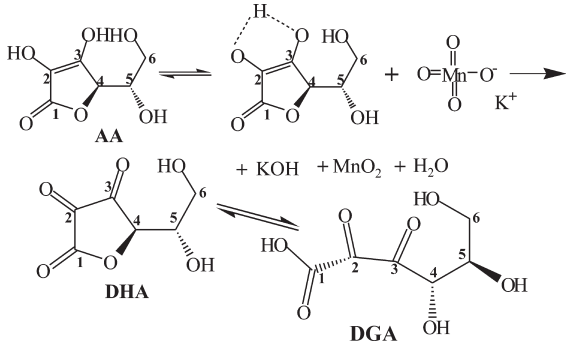

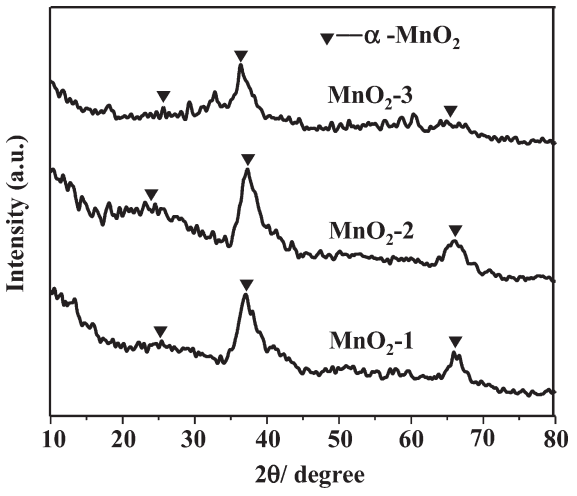

Figure 1. Powder XRD patterns of as-prepared MnO_2-1, MnO_2-2, and MnO_2-3.

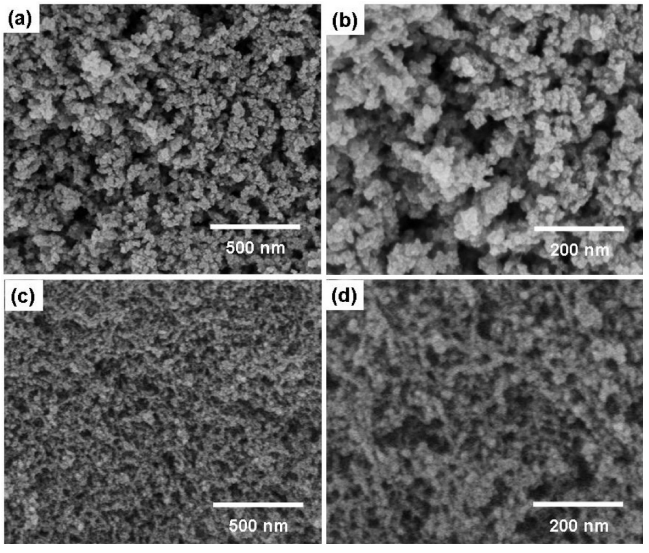

Figure 2. SEM images of as-prepared MnO_2-1 (a,b) and MnO_2-3 (c,d).

Table 2. Texture Parameters of AC and MnO_2 Prepared under Different Experimental Conditions

sample	crystal phase	crystallite size[a] (nm)	S_{BET}[b] ($m^2\ g^{-1}$)	V_{total}[c] ($m^3\ g^{-1}$)	D_{peak}[d] (nm)	C[e] ($F\ g^{-1}$)	CE[f] (%)
MnO_2-1	α-MnO_2	10	202	0.71	12.6	170	95
MnO_2-2	α-MnO_2	5	247	0.49	6.5	175	94
MnO_2-3	α-MnO_2	4	284	0.72	8	190	95
MnO_2-4	α-MnO_2	9	222	0.67	9.3	200	95
MnO_2-5	α-MnO_2	20	198	0.51	8.3	135	104
MnO_2-6	α-MnO_2	8	264	0.72	8	160	95
MnO_2-7	α-$MnO_2$and Mn_2O_3	14	103	0.97	10.1	140	96
MnO_2-8	Mn_2O_3	16	104	0.86	11	110	102
AC[g]			1869	0.93	1	160	99

[a] Crystallite sizes were calculated by the Scherrer formula. [b] BET specific surface area was calculated over the P/P_0 range 0.03 to 0.25. [c] Total pore volume at $P/P_0 \sim 0.995$. [d] The maximum BJH pore size distribution peak. [e] The specific gravimetric capacitance measured by the galvanostatic charge−discharge at a current density of 6.0 mA cm^{-2}. [f] Columbic efficiency. [g] Commercial activated carbon (YP/47, Japan).

dx.doi.org/10.1021/jp110938x |J. Phys. Chem. C 2011, 115, 5413–5421

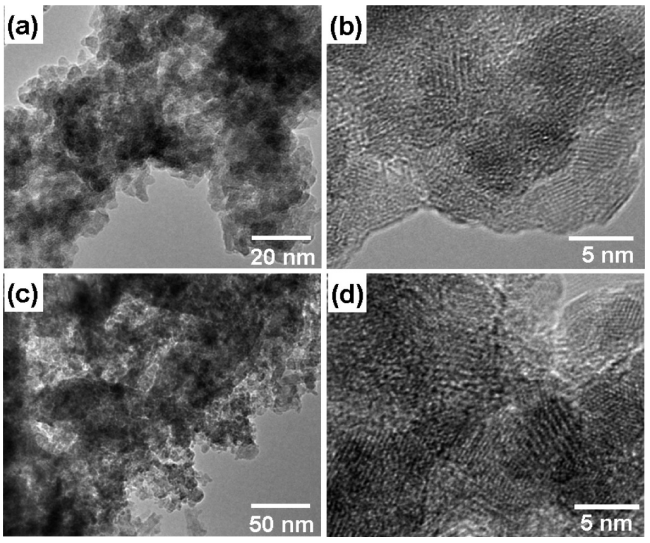

Figure 3. HRTEM images of MnO_2-2 (a,b) and MnO_2-3 (c,d).

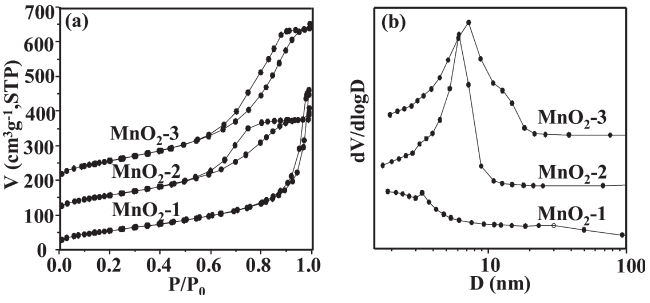

Figure 4. N_2 sorption isotherms (a) and pore size distributions (b) of MnO_2 prepared with different mole ratios of $KMnO_4$ to ascorbic acid. The isotherms of MnO_2-2 and MnO_2-3 were offset by 90 and 180 $cm^3\ g^{-1}$ STP, respectively.

of the nanocrystals after all monomers were consumed should decrease as the concentration of ascorbic acid is increased since the $KMnO_4$ concentration was fixed.

To get more structural information about the products, samples MnO_2-2 and MnO_2-3 were characterized with HRTEM, and their representative images are displayed in Figure 3. It can be clearly seen that the MnO_2 samples comprise of small nanoparticles with size ca. 5 nm. This observation is basically consistent with the XRD results. These small nanoparticles further constructed three-dimensional frameworks with abundant mesopores in between the primary MnO_2 nanoparticles. The presence of mesopores is also confirmed by nitrogen adsorption analysis, as shown in Figure 4. The mesopores may be beneficial for ionic transportation through the electrolyte to enhance the electrochemical performance.

As shown in Figure 4, the nitrogen sorption isotherm of the resultant MnO_2-1 exhibits a hysteresis loop in the relative pressure range above 0.90, and no plateau appears in the adsorption branch, indicating the existence of macropores. The nitrogen sorption isotherms of MnO_2-2 and MnO_2-3 are of type IV, displaying a hysteresis loop in the relative pressure range of 0.6−0.90, and plateaus appeared in the adsorption branch, indicating the purely mesoporous nature. These results are in agreement with HRTEM and SEM observations. The calculated

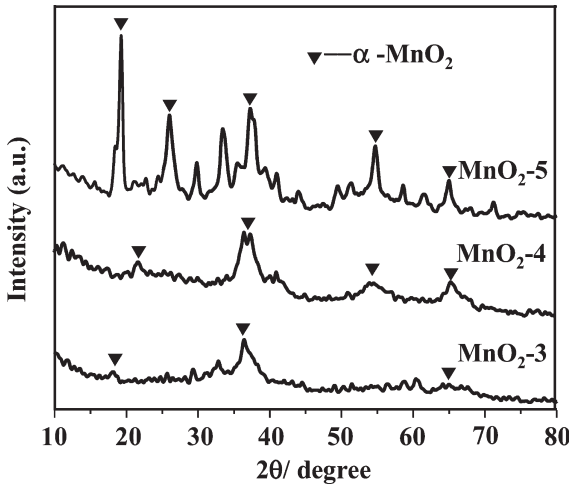

Figure 5. Powder XRD patterns of as-prepared MnO_2-3, MnO_2-4, and MnO_2-5.

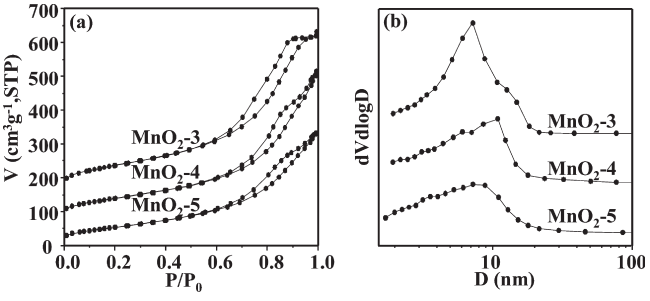

Figure 6. N_2 isotherms (a) and pore size distributions (b) of MnO_2 samples collected at different reaction times from 10 to 60 min. The isotherms of MnO_2-4 and MnO_2-3 were offset by 80 and 160 $cm^3\ g^{-1}$ STP, respectively.

texture parameters of these MnO_2 nanoparticles are compiled in Table 2. It can be seen that the product MnO_2-2 and MnO_2-3 possess higher BET surface areas (up to 284 $m^2\ g^{-1}$) than that of MnO_2-1 (202 $m^2\ g^{-1}$). Samples MnO_2-2 and MnO_2-3 have narrow pore size distributions with mesopore sizes concentrated at ca. 7 nm.

3.2. Effect of the Reaction Time on the Structure of MnO_2. Keeping a molar ratio of $KMnO_4$ to ascorbic acid of 1:1, reaction times of 10, 30, and 60 min were investigated. The crystal phase and particle size of the as-prepared MnO_2 were characterized by powder XRD. As seen in Figure 5, the XRD patterns of the as-prepared MnO_2 nanoparticles can also be assigned to the α-MnO_2 phase. The reflection of MnO_2-3 is much broader than that of MnO_2-4, while MnO_2-5 is the sharpest. The crystallite sizes of the MnO_2 particles calculated by the Scherrer formula are also compiled in Table 2. It indicates that the particle size of MnO_2-3 is the smallest, MnO_2-4 is the second, and MnO_2-5 is the largest.

The MnO_2 obtained was also characterized by N_2 sorption. The isotherms and corresponding pore size distributions are displayed in Figure 6. As seen, all the isotherms are also of type IV and exhibit hysteresis loops in the relative pressure range of 0.7−0.95, indicating these materials are mesoporous. The pore size distributions show that the products MnO_2-3, MnO_2-4, and MnO_2-5 have mesopore size concentrated at ca. 8.0 nm. As

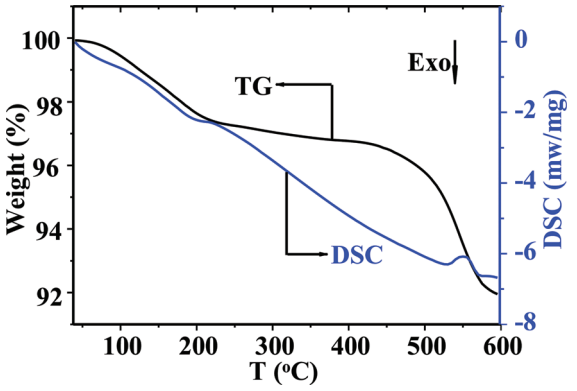

Figure 7. TG and DSC curves of as-prepared MnO_2-3.

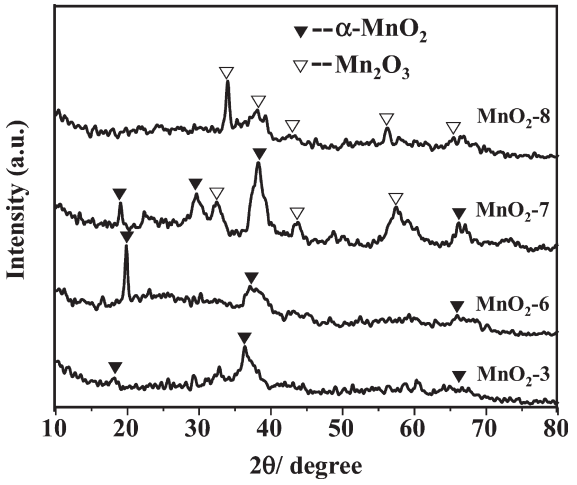

Figure 8. Powder XRD patterns of as-prepared sample MnO_2-3 and its calcined samples (MnO_2-6, MnO_2-7, and MnO_2-8 were calcined at temperatures of 200, 300, and 400 °C, respectively).

shown in Table 2, sample MnO_2-3 exhibits the highest surface area.

3.3. Thermal Stability of the Prepared MnO_2. The phase structure of the as-prepared MnO_2 is usually unstable during the long-period electrochemical cycles if this material is directly used as electrode without any thermal treatment. However, a thermal treatment always causes a loss of surface area and transfer of phase structure. Therefore, it is necessary to find an optimal thermal treatment condition in order to maintain the prepared MnO_2 α phase and suitable surface area.

First, the thermal decomposition behavior of MnO_2 was analyzed and the TG/DSC curves of the as-prepared MnO_2-3 are displayed in Figure 7. As shown, this sample shows ca. 2% weight loss upon heating from room temperature to 200 °C, which is accompanied by a small endothermic peak at approximately 200 °C, indicating the loss of water molecules which exist both on the surface and in the lattice of the nanostructure. In fact, a considerable amount of water content is essential for an electrode material as it is conducive for ionic transportation in an electrolyte, thus enhancing electrochemical performance.[24] Therefore, the water loss upon heat treatment can be considered as detrimental for electrochemical properties of MnO_2. Subsequently, a slight weight loss less than 1% occurs in the temperature range of 200−450 °C. Finally, a weight loss of 4% appeared

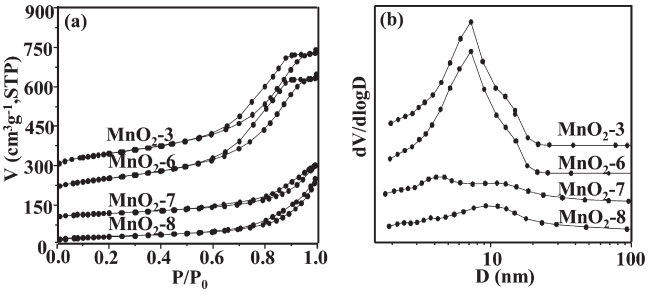

Figure 9. Nitrogen isotherms (a) and pore size distributions (b) of the as-prepared and calcined MnO_2 samples. The isotherms of MnO_2-7, MnO_2-6, and MnO_2-3 were offset vertically by 90, 180, and 270 cm^3/g STP, respectively.

after the temperature is higher than 450 °C, and a sharp endothermic peak was found at approximately 550 °C.

Following the TG/DSC analysis, sample MnO_2-3 was calcined at temperatures of 200, 300, and 400 °C, for 2 h to investigate its phase transformation. Figure 8 shows the XRD patterns of the calcined samples. It can be seen that sample MnO_2-6 calcined at 200 °C still remains as α-MnO_2, indicating that dehydration of the as-prepared oxide did not cause damage to the crystal structure. Sample MnO_2-7 calcined at 300 °C was subjected to a crystal phase transformation, which consists of α-MnO_2 and Mn_2O_3, indicating that the sample is essentially a mixture. Further increasing the calcination temperature to 400 °C shows that the obtained sample MnO_2-8 was completely converted to Mn_2O_3.

The nitrogen sorption isotherms and the pore size distributions are shown in Figure 9. The isotherm of sample MnO_2-6 with a hysteresis loop at the relative pressure (P/P_0) range of 0.7−0.95 is quite similar to that of MnO_2-3, indicating the porous structure of MnO_2 is essentially unchanged. With increasing calcination temperature, the isotherms of MnO_2-7 and MnO_2-8 are still of type IV; however, the hysteresis loops progressively decrease and move to higher relative pressure, which reflects the formation of large mesopores or macropores. The sorption volume also gradually decreases, corresponding to a lower surface area and pore volume (see Table 2). Pore size distributions of MnO_2 show that the sample MnO_2-6 exhibits a concentrated pore size distribution in the range of 6−8 nm, which is basically the same as that of MnO_2-3, while the samples MnO_2-7 and MnO_2-8 have wide pore size distributions. Obviously, the as-prepared MnO_2-3 is suitable for thermal treatment at 200 °C. The resultant MnO_2-6 retains not only a high surface area but also an unchanged crystalline structure.

3.4. Electrochemical Performance of MnO_2. There are two proposed mechanisms for the charge storage in a MnO_2 electrode.[25] One involves adsorption/desorption of protons H_3O^+ or cations M^+ from the electrolyte.

$$(MnO_2)_{surface} + M^+ + e^- \leftrightarrow (MnO_2{}^-M^+)_{surface}$$
$$M^+ = (Li^+, Na^+, K^+, \text{ or } H_3O^+)$$

This mechanism mainly describes a surface process, which involves the adsorption/desorption of alkali cations. It is likely to be predominant in amorphous MnO_2. Another mechanism is based on intercalation/deintercalation of H^+ or alkali cations such as Li^+, Na^+, and K^+, etc. into the bulk oxide particles with concomitant reduction/oxidation of the manganese cations. The second mechanism is believed to be predominant in crystalline

dx.doi.org/10.1021/jp110938x |J. Phys. Chem. C 2011, 115, 5413–5421

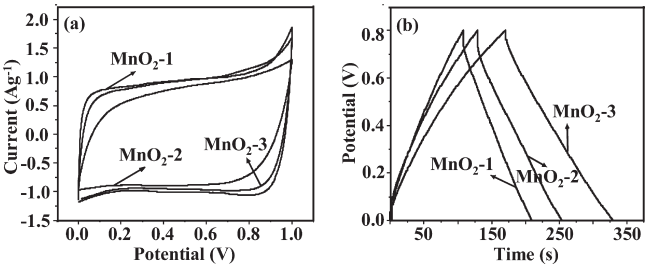

Figure 10. Cyclic voltammograms in 0.5 M Na_2SO_4 at a scan rate of 5 mV s^{-1} (a) and charge−discharge curves of the first 10 cycles at a constant current density of 6 mA cm^{-2} (b) of MnO_2 nanoparticles prepared with different mole ratios of $KMnO_4$ to ascorbic acid.

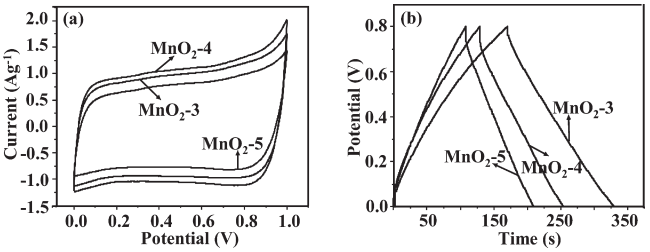

Figure 11. Cyclic voltammograms in 0.5 M Na_2SO_4 at a scan rate of 5 mV s^{-1} (a). Charge−discharge curves of the first 10 cycles at a constant current density of 6 mA cm^{-2} (b) of nano-MnO_2 samples collected at different reaction times.

MnO_2. In this case, the bulk oxide particles with well-developed interconnectivity would be helpful in terms of the ion transfer of the electrolyte.

$$MnO_2 + H^+ + e^- \leftrightarrow MnOOH$$

$$\text{or} MnO_2 + M^+ + e^- \leftrightarrow MnOOMM^+ = (Li^+, Na^+, K^+, \text{ or } H_3O^+)$$

Our synthesized α-MnO_2 samples as electrode materials were tested by cyclic voltammetry (CV) and constant current charge/discharge tests. Figure 10a shows CV plots recorded for the MnO_2-1, MnO_2-2, and MnO_2-3 in 0.5 M Na_2SO_4 electrolyte at a scan rate of 5 mV s^{-1} and in a potential range of 0 −1.0 V. It can be seen that there are no sharp redox peaks over the potential range investigated. The rectangular voltammograms suggest an ideal capacitive behavior of the as-prepared MnO_2. This may benefit from the three-dimensional framework, which results in a lower series resistance due to open transport paths and a greater access of the electrolyte to the active surface of manganese dioxide. Typical charge−discharge curves in Figure 10b reveal that the as-prepared MnO_2 exhibits stable electrochemical behavior as the capacitor voltage varies linearly with time during the charging and discharging process. This type of linear variation of potential is another important criterion for capacitance behavior of an electrode material. The calculated specific capacitance of the as-prepared MnO_2 is shown in Table 2. We can see that the greater the amount of ascorbic acid used, the higher the capacitance of the MnO_2

The CV and charge−discharge curves using MnO_2 nanoparticles as the electrode materials that were prepared under different reaction times are compiled in Figure 11a, and the calculated specific capacitance is listed in Table 2. We can see that as the reaction time increases, the capacitance declines with a decrease in specific surface area. The sample MnO_2-4 exhibits a maximum specific capacitance (200 F g^{-1}) at a current density of 6.0 mA cm^{-2} which is comparable with the reported values for MnO_2 or other metal oxide nanoparticles (Table 3 summarizes the literature data on the electrochemical performance of MnO_2 compounds as electrochemical supercapacitors). Galvanostatic charge−discharge cycling data of the nano-MnO_2 electrode at the same current density are shown in Figure 11b. The variation of potential with time is linear during both charging and discharging.

Considering the possible effect of the inside temperature of storage devices on the efficiency and safety of the operating electrode, it is important to ensure active materials capable of maintaining the original structure even at high temperatures. Thus, the sample marked as MnO_2-3 was calcined at various temperatures (200, 300, and 400 °C) for 2 h to investigate its thermal transformation. The results of cyclic voltammetry and constant current charge/discharge tests are shown in Figure 12. It can be seen that all the samples still retain the approximate rectangle CV shaped curves and the linear variation of potential with time. In the current study, 200 °C is the most suitable temperature for the activation of electrode material.

Specific capacitance values for MnO_2 samples heated at different temperatures are listed in Table 2. There is a slight decrease in specific capacitance for the samples heated at 200 °C compared to the original as-prepared MnO_2-3. However, for the samples heated at 300 and 400 °C, gradual decreases in specific capacitance are visible due to the decrease in specific surface area. A similar trend is found in the RuO_2 capacitor behavior.[26] When the samples are treated at lower temperatures, the as-prepared MnO_2 with more adsorbed water and chemical hydration water has a hydrophilic surface structure, which can improve the protons/ions diffusion and adsorption/desorption during the redox transitions so that more protons will insert into the electrode material surface or inside to participate in the redox reactions. Though a small amount of water is good for improving the electrode material activity, the inner resistance is another consideration for the comprehensive electrochemical properties. In this study, 200 °C is a suitable temperature for the activation of electrode material.

The supercapacitive property of the sample MnO_2-6 was further tested by CV at different scan rates. The CV plots (Figure 13a) at all scan rates are close to a rectangular shape with a mirror-image feature even at the scan rate of 50 mV s^{-1}. For comparison, the MnO_2 synthesized using the common fluid phase method with potassium permanganate and manganous acetate (denoted as FP-MnO_2, α-MnO_2, and S_{BET} = 173 m^2 g^{-1}; more information can be obtained in Figure S1 in the Supporting Information) was used as electrode, and the electrochemical performance was also tested. Obviously, the CV curves are becoming distorted with the increase of the scan rate (Figure 13b), indicating that the electrode has distinctly polarized. The excellent supercapacitive properties of resultants can be attributed to their unique microstructure and crystal structure. First, the prepared MnO_2 microstructure possesses an extremely large surface area. Second, the crystal structure of the prepared α-MnO_2 is constructed from double chains of octahedral $[MnO_6]$ which form the (2×2) tunnels with a cavity as large as 0.46 nm. Last, but most important, is the three-dimensional frameworks which have abundant mesopores. This unique microstructure can shorten the diffusion distance for ions, facilitate ionic

Table 3. Summary of Electrochemical Data of MnO_2 or Other Metal Oxide Electrodes [a]

ref	microstructure	XRD	S_{BET} (m^2 g^{-1})	C (F g^{-1})	v (mV/s)	electrolyte
3		$RuO_2 \cdot xH_2O$	25−95	720	2	2 M H_2SO_4
5	high surface area materials	α-MnO_2	180	166	2	0.1 M Na_2SO_4
8	hollow spheres	α-MnO_2	108.6	147	5	1 M Na_2SO_4
9	nanoporous materials	α-MnO_2	283	309	5	1 M Na_2SO_4
		NiO	179	165		
13	single-crystal nanorods	α-MnO_2		70.9	5	0.5 M Na_2SO_4
16	monodisperse 3D nanoflowers	crystalline MnO_2	225.9	121.5	5	1 M LiOH
17	5 μm particles	amorphous MnO_2	83	110	5	2 M NaCl
18	nanoparticles and nanorods	α-MnO_2		250	0.5	0.1 M Na_2SO_4
25	plate-like surface with nanorods	α-MnO_2	132	168	5	2 M Na_2SO_4
this study	nanostructure mesoporous with 3D frameworks	α-MnO_2	222	200	5	0.5 M Na_2SO_4

[a] Complete data set can be found in the related papers.

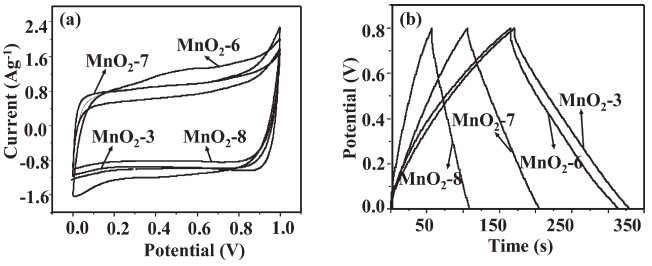

Figure 12. Cyclic voltammograms in 0.5 M Na_2SO_4 at a scan rate of 5 mV s^{-1} (a). Charge−discharge curves of the first 10 cycles at a constant current density of 6 mA cm^{-2} (b) of nano-MnO_2 samples calcined at different temperature.

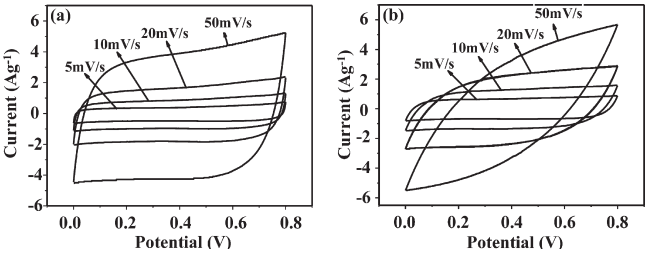

Figure 13. CV curves of sample MnO_2-6 (a) and FP-MnO_2 in the potential range from 0 to 0.8 V at different scan rates.

transportation through the electrolyte, and hence improve the electrochemical performance. All of these features can make the materials more attractive as electrodes in supercapacitors.

3.4. Electrochemical Performance of Hybrid AC-MnO_2&AC Capacitor. From the foregoing experiments, it was shown that 200 °C is the most suitable temperature for the activation of electrode material. Therefore, the sample MnO_2-6 was selected as the positive material to fabricate a hybrid supercapacitor where AC was used as the negative electrode. In order to improve the electrical conductivity of the MnO_2 positive electrode material and achieve a high capacitance, we utilize a certain amount of activated carbon (AC) to mix with MnO2, wherein the AC has the dual function of both a conductive agent and an active substance of a positive electrode. Thus, the fabricated hybrid supercapacitor is composed of MnO_2 and AC (MnO_2&AC) as the positive electrode and AC as the negative electrode, which integrates approximate symmetric and asymmetric behaviors in

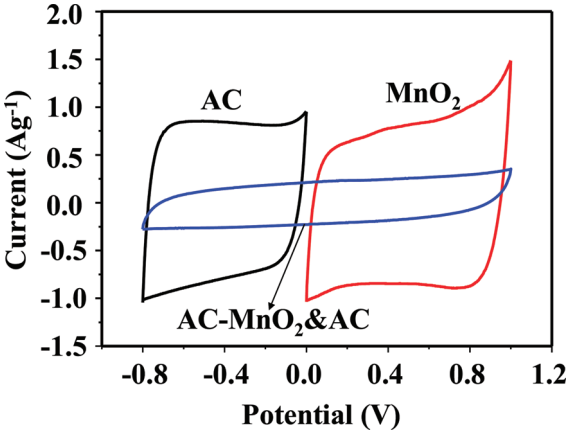

Figure 14. Cyclic voltamogramms of AC, MnO_2, and an optimized hybrid AC-MnO_2&AC capacitor in 0.5 M Na_2SO_4 aqueous solution at a scan rate of 5 mVs^{-1}.

the distinct parts of 1.8 V operating windows.[27,28] That is, MnO_2 in the positive electrode and AC in the negative electrode together form a pure asymmetric structure, which extends the operating voltage to 1.8 V due to the compensatory effect of opposite overpotentials. In the range of −0.8−0 V, both ACs in the positive and negative electrodes assemble as a symmetric structure via a parallel connection which offers more capacitance and less internal resistance. The weight ratio of AC to MnO_2 was fixed at ∼1:7 according to charge balance assuming the specific capacitance of the AC electrode is 160 F g^{-1} and the MnO_2 electrode is 160 F g^{-1}. The hybrid supercapacitor AC-MnO_2&AC was tested in 0.5 M Na_2SO_4 aqueous electrolyte. Figure 14 shows the CV curves of the individual electrode vs SCE reference electrode and the hybrid AC-MnO_2&AC aqueous supercapacitor at a scan rate of 5 mVs^{-1}. The CV curve of the AC negative electrode shows an ideal rectangular shape without noticeable redox peaks from −0.8 to 0 V. This is a characteristic of charging/discharging of an electric double layer capacitance. In the potential range of 0−1.0 V, the performance of the MnO_2 positive electrode deviates slightly from the ideal rectangular shape, indicating a pseudocapacitance behavior. Moreover, the CV curve of the MnO_2 electrode is symmetric with respect to the zero-current axis, revealing that reversible faradic reactions took place in MnO_2. Hence, a hybrid AC-MnO_2&AC supercapacitor can be fabricated using Na_2SO_4 solution as the electrolyte, MnO_2

dx.doi.org/10.1021/jp110938x |J. Phys. Chem. C 2011, 115, 5413–5421

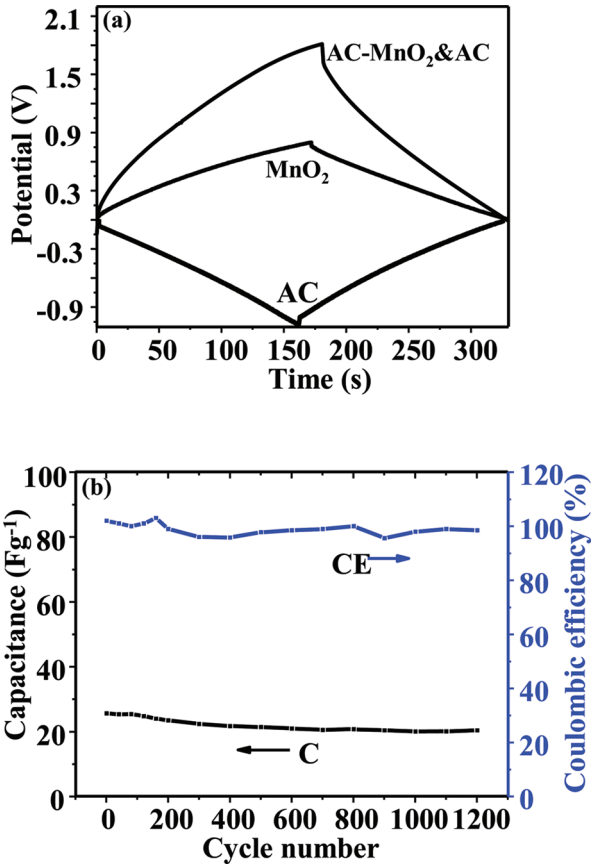

Figure 15. Potential vs time curves of the individual electrode vs SCE reference electrode and the voltage vs time profile of the hybrid AC-MnO_2&AC aqueous supercapacitor in 0.5 M Na_2SO_4 electrolyte (a). Cycling behavior of the hybrid AC/0.5 M Na_2SO_4/MnO_2&AC aqueous supercapacitor at a current density of 12.74 mA cm^{-2} between 0 and 1.8 V (b).

nanoparticles, and activated carbon as the positive and negative electrodes, respectively. We can see that the asymmetric supercapacitor shows a sloping voltage profile from 0 to 1.8 V with excellent reversibility, and its specific discharge capacitance can be as high as 23.1 F g^{-1} based on the total mass of the two active electrode materials.

Figure 15a shows the potential vs time curves of the individual electrode vs SCE reference electrode and the voltage vs time profile of the hybrid AC-MnO_2&AC aqueous supercapacitor at a current density of 12.74 mA cm^{-2}. The potential of the AC cathode shows a typical linear relationship with time, a characteristic of an electric double layer capacitance. The potential vs time curves of the MnO_2 anode also exhibit an almost linear shape due to its fast pseudocapacitive nature. The hybrid supercapacitor shows a sloping voltage profile from 0 to 1.8 V with excellent reversibility.

Figure 15b shows the cycling behavior of the hybrid AC-MnO_2&AC supercapacitor in 0.5 M Na_2SO_4 electrolyte at a current density of 12.74 mA cm^{-2} between 0 and 1.8 V. The supercapacitor shows good cycling behavior with 23.1 F g^{-1} maintained after 1000 cycles, which was calculated on the basis of the total mass of the two active electrode materials. The calculated maximum energy density and power density are of 10.4 Wh kg^{-1} and 14.7 kW kg^{-1} after 1200 cycles, respectively. We can see a significant decline in the beginning of the first 200 cycles, which may be due to the activation and stability process of the electrode gradually reaching a steady-state. Here, we did not take any measures to remove the dissolved oxygen from the electrolyte in our tests. In fact, this will make the cycling stability of the electrodes worse.[29] The coulombic efficiency of the capacitor remains at 100% except in the first several cycles, suggesting that no gas evolution occurred in this voltage range. This good behavior is due to the unique chain-like structure with abundant mesopores embedded in the electrode materials.

4. CONCLUSIONS

We have synthesized a series of mesoporous manganese dioxide nanoparticles through the one-pot reaction of $KMnO_4$ and ascorbic acid under ambient conditions. The resultants exhibit a few interesting characteristics such as mesoporous structure, high surface area, narrow mesopore size distribution, and three-dimensional frameworks. Electrochemical studies reveal that using the nanosized mesoporous MnO_2 as an electrode material, the capacitance achieved can be as high as up to 200 F g^{-1}. Furthermore, a hybrid supercapacitor AC-MnO_2&AC can be fabricated, which exhibited a high capacitance of 23.1 F g^{-1}, a maximum energy density of 10.4 Wh kg^{-1}, and a power density of 14.7 kW kg^{-1} after 1200 cycles. Thus, manganese oxide nanoparticles prepared by the room temperature reduction of $KMnO_4$ with ascorbic acid show good electrochemical performance, which can be used as a positive electrode material in a hybrid supercapacitor.

■ ASSOCIATED CONTENT

Supporting Information. Powder XRD pattern, SEM image, nitrogen sorption isotherm and cyclic voltammograms of FP-MnO_2. This material is available free of charge via the Internet at http://pubs.acs.org.

■ AUTHOR INFORMATION

Corresponding Author

*Tel/Fax: +86 411 84986122. E-mail: wencuili@dlut.edu.cn.

■ ACKNOWLEDGMENT

We thank the financial support by Program for New Century Excellent Talents in University of China (NCET-08-0075) and the National Natural Science Foundation of China (No.20973031). We are grateful to Mr. B. Spliethoff for TEM measurements.

■ REFERENCES

(1) Conway, B. E. *J. Electrochem. Soc.* **1991**, *138*, 1539–1548.
(2) Conway, B. E.; Birss, V.; Wojtowicz, J. *J. Power Sources* **1997**, *66*, 1–14.
(3) Zheng, J. P.; Jow, T. R. *J. Electrochem. Soc.* **1995**, *142*, L6–L8.
(4) Kötz, R.; Carlen, M. *Electrochim. Acta* **2000**, *45*, 2483–2498.
(5) Toupin, M.; Brousse, T.; Belanger, D. *Chem. Mater.* **2002**, *14*, 3946–3952.
(6) Hu, C.-C.; Tsou, T.-W. *Electrochem. Commun.* **2002**, *4*, 105–109.
(7) Devaraj, S.; Munichandraiah, N. *J. Phys. Chem. C* **2008**, *112*, 4406–4417.
(8) Xu, M.; Kong, L.; Zhou, W.; Li, H. *J. Phys. Chem. C* **2007**, *111*, 19141–19147.

(9) Yu, C.; Zhang, L.; Shi, J.; Zhao, J.; Gao, J.; Yan, D. *Adv. Funct. Mater.* **2008**, *18*, 1544–1554.
(10) Liu, R.; Lee, S. B. *J. Am. Chem. Soc.* **2008**, *130*, 2942–2943.
(11) Fei, J. B.; Cui, Y.; Yan, X. H.; Qi, W.; Yang, Y.; Wang, K. W.; He, Q.; Li, J. B. *Adv. Mater.* **2008**, *20*, 452–456.
(12) Chen, H.; He, J. *J. Phys. Chem. C* **2008**, *112*, 17540–17545.
(13) Wang, H.; Lu, Z.; Qian, D.; Li, Y.; Zhang, W. *Nanotechnology* **2007**, *18*, 115616.
(14) Jeong, Y. U.; Manthiram, A. J. *Electrochem. Soc.* **2002**, *149*, A1419–A1422.
(15) Toupin, M.; Brousse, T.; Bélanger, D. *Chem. Mater.* **2004**, *16*, 3184–3190.
(16) Ni, J.; Lu, W.; Zhang, L.; Yue, B.; Shang, X.; Lv, Y. *J. Phys. Chem. C* **2008**, *113*, 54–60.
(17) Reddy, R. N.; Reddy, R. G. *J. Power Sources* **2004**, *132*, 315–320.
(18) Ragupathy, P.; Vasan, H. N.; Munichandraiah, N. *J. Electrochem. Soc.* **2008**, *155*, A34–A40.
(19) Ching, S.; Landrigan, J. A.; Jorgensen, M. L. *Chem. Mater.* **1995**, *7*, 1604–1606.
(20) Chen, H.; He, J.; Zhang, C.; He, H. *J. Phys. Chem. C* **2007**, *111*, 18033–18038.
(21) Jana, N. R.; Gearheart, L.; Murphy, C. J. *Langmuir* **2001**, *17*, 6782–6786.
(22) Zhang, D.; Qi, L.; Yang, J.; Ma, J.; Cheng, H.; Huang, L. *Chem. Mater.* **2004**, *16*, 872–876.
(23) Bode, A.; Cunningham, L.; Rose, R. *Clin. Chem.* **1990**, *36*, 1807–1809.
(24) Thackeray, M. M. *Prog. Solid State Chem.* **1997**, *25*, 1–71.
(25) Subramanian, V.; Zhu, H.; Wei, B. *J. Power Sources* **2006**, *159*, 361–364.
(26) Lin, C.; Ritter, J. A.; Popov, B. N. *J. Electrochem. Soc.* **1999**, *146*, 3155–3160.
(27) Gao, P. C; Lu, A. H.; Li, W. C. *J. Power Sources* **2011**, *196*, 4095–4101.
(28) Khomenko, V.; Raymundo-Piñero, E.; Béguin, F. *J. Power Sources* **2006**, *153*, 183–190.
(29) Brousse, T.; Taberna, P.-L.; Crosnier, O.; Dugas, R.; Guillemet, P.; Scudeller, Y.; Zhou, Y.; Favier, F.; Bélanger, D.; Simon, P. *J. Power Sources* **2007**, *173*, 633–641.